Light Control over Chirality Selective Functionalization of Substrate Supported Carbon Nanotubes

Georgy Gordeev,[*,#] Thomas Rosenkranz,[#] Frank Hennrich, Stephanie Reich, and Ralph Krupke[*]

ABSTRACT: Diazonium reactions with carbon nanotubes form optical sp^3 defects that can be used in optical and electrical circuits. We investigate a direct on-device reaction supported by confined laser irradiation and present a technique where an arbitrary carbon nanotube can be preferentially functionalized within a device by matching the light frequency with its transition energy. An exemplary reaction was carried out between (9,7) nanotube and 4-bromobenzenediazonium tetrafluoroborate. The substrate supported nanotubes of multiple semiconducting chiralities were locally exposed to laser light while monitoring the reaction kinetics *in situ* via Raman spectroscopy. The chiral selectivity of the reaction was confirmed by resonant Raman spectroscopy, reporting a 10 meV E_{22} transition energy red-shift only of the targeted species. We further demonstrated this method on a single tube (9,7) electroluminescent device and show a 25 meV red-shifted emission of the ground state E_{11} compared to the emission from the pristine tubes.

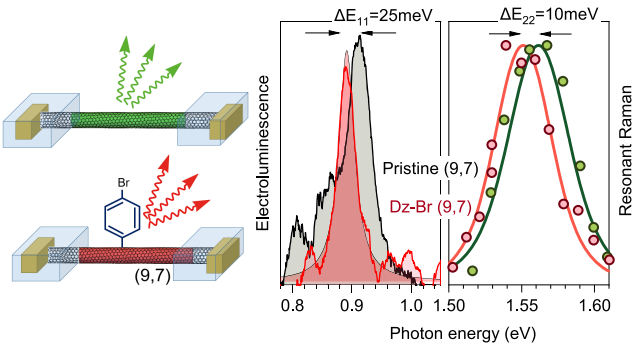

INTRODUCTION

Single-walled carbon nanotubes (SWCNTs) are unique one-dimensional crystals with outstanding mechanical, optical, and electrical properties.[1,2] The properties of the CNTs could be improved by introducing functional groups onto the CNT surface. Such functionalization can improve intrinsic CNT properties,[3] merge CNT properties with those of functional moiety,[4] or even create new optical states via defect engineering.[5,6] The most robust approach is covalent functionalization where a chemical bond is created between functional moieties and the CNT. Recently tremendous attention has been paid to covalent functionalization techniques with aryl,[5] alkane,[7] and epoxide[8] groups because they enable precise control over the defect type and yield novel properties. For fully harvesting such properties in devices, the functionalized CNTs require a reliable integration into electrical and photonic circuits.[9−11] There are two possible pathways, either the CNT is functionalized before or after integration. While the first method is applicable for a standard solution processed material, the lateral position of the functional group is not well controlled and might occur not at the center of a cavity or between electrodes but somewhere close to a contact, where optical emission can be suppressed. An alternative approach is to functionalize CNTs directly on a device. For this novel approach a functionalization reaction must be developed for substrate supported configurations.

The reaction between CNTs and diazonium salts (Dz)[12−14] is sensitive to visible light.[7,15−17] Aryl ring functionalization first occurs in metallic CNTs, which has been used to enrich CNTs of electronic type.[12,18] In semiconducting CNTs the reaction is inherently slow and can take weeks to succeed, but when light drives the reaction, it accelerates to a just few hours.[16] This activation process is more effective with photons whose energy matches absorption[16,17] occurring at optical transitions E_{11}, E_{22}, etc.[1] The transition energies of the CNT are determined by the (n,m) chirality, therefore offering a pathway for chiral selectivity. Light driven reactions were so far only performed in bulk aqueous[5,7,16] and organic solutions[19] and dried films.[20] The questions remain of whether an on-device reaction occurs at a liquid−solid phase boundary, given the limited amount of access points, and whether the reaction at the surface is still light sensitive and chirality selective. Another challenge is that reaction monitoring by the optical signatures of defect states may be inaccessible in devices. We therefore need to find visible alternatives, such as electrical performance, vibrational spectroscopy, or changes in the energies of the delocalized excitons.

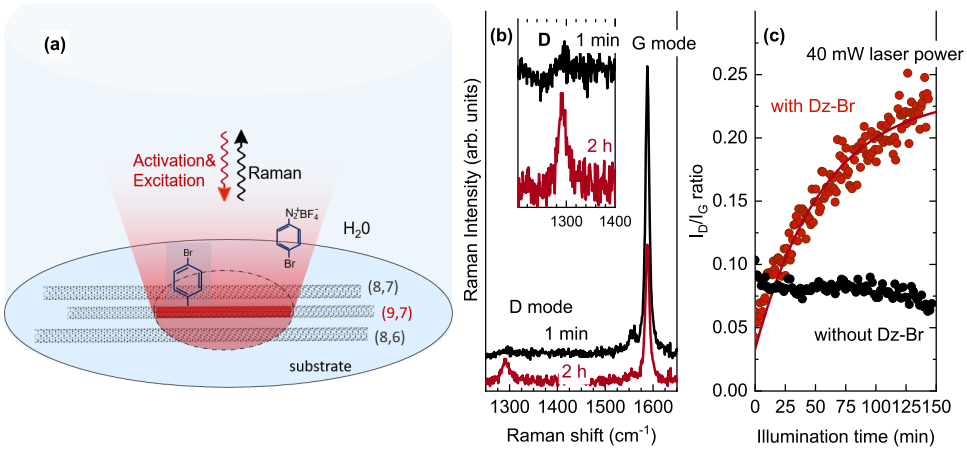

Figure 1. Experimental setup for laser assisted functionalization. (a) Experimental scheme. The nanotubes were drop casted onto the substrate and covered with the aqueous solution. The activation laser of 785 nm (1.58 eV) is focused onto the CNTs, and backscattered light is analyzed with a Raman spectrometer. After addition of the Dz-Br to the solution the functionalization proceeds with the CNT resonant with activation light (highlighted by a red color). (b) Examples of the Raman spectra collected during reaction (black) at the start and (red) after addition of Dz-Br and 2 h illumination. The inset shows the magnified region of the D mode. (c) Reference measurement: evolution of the D/G ratio as a function of 40 mW illumination time (black) without addition of Dz-Br and (red) with addition.

The monitoring of the reaction *in situ* is crucial for understanding the reaction kinetics and the physical effects of functionalization such as strain or doping. The evolution of Raman spectra can be used to monitor the reaction *in situ*. The covalent bond formation is accompanied by the sp^3 distortion in the sp^2 hybridized CNT lattice. This distortion breaks the translational symmetry and introduces a defect state.[21] Thus, the selection rules for momentum forbidden Raman scattering processes change. The defect induced modes occur at ∼1300−1350 cm^{-1} in most sp^2 carbons, including graphite,[22] graphene,[23,24] and CNTs.[21] The D mode has been widely used in functionalized materials,[14,25] including aryl ring functionalization.[18] The increase of the D mode can therefore serve as a scale of the reaction product, since it is proportional to the concentration of defects. An additional doping effect, imposed by a functional group, can also be detected via Raman spectroscopy.[26] The expected changes in the G mode positions of semiconducting CNTs are on the order of 0.5 cm^{-1} [27] and are difficult to analyze *ex situ*.

Our manuscript consists of three sections in Results. In the first we study the reaction kinetics and light sensitivity on a mixed chirality sample. From all chiralities we target (9,7) CNT with a 1.58 eV laser and monitor *in situ* evolution of the Raman modes. We determine the influence of the photon flux on the reaction rates and products. Further, we investigate the functionalization spot and find the defects exclusively in the areas irradiated by light. In the second section we investigate chiral selectivity. The transition energy shifts of three CNT species are investigated by resonance Raman spectroscopy. The red-shift is only found in the targeted (9,7) CNT. With this we establish an additional transition-energy-based metric of functionalization. In the third section, we apply this metric for a single-tube electroluminescence device.[28] The functionalization occurs after CNT integration onto a device, and its spectral output indicates a successful reaction together with a change of electrical transport characteristics.

EXPERIMENTAL METHODS

The very first step is the preparation of the semiconducting CNTs suspension. The nanotubes need to be purified first in order to remove all metallic species. The HiPco-CNT suspensions in toluene were prepared using the polymer wrapping technique.[29] The poly(9,9-di-*n*-octylfluorenyl-2,7-diyl) (PFO) provided from Sigma-Aldrich was used as a polymer surfactant. The excess polymer was removed with the help of size-exclusion chromatography (SEC).[30] The suspensions contain μm-long s-CNTs with almost no m-CNTs and low polymer concentration.

We found that with laser-assisted functionalization (LAF) it is possible to select the desired chirality and use scattered light for monitoring reaction *in situ*. The DzBr salt was purchased from Sigma-Aldrich, with a molecular weight of 270.82 g/mol and 96% purity yielding a concentration of 3.5 μmol/g when 1 mg is dissolved in 1 g of water. The freshly prepared solution has a pH value of 3.6. For the laser-assisted functionalization, the DzBr solution was diluted (1:100) to a concentration of 35 nmol/g for exposure to the nanotube.

For the experimental setup for *in situ* monitoring of functionalization, a schematic view of the laser-assisted kinetic measurements is given in Figure 1a. The substrate was placed in a plastic container for the LAF step. The drop casted CNTs were covered with 2 mL of deionized water and a glass cover floating on the droplet to overcome the lens effect at the water surface. The measurements were done with excitation powers between 2 and 40 mW with a 5× objective resulting in a power density from 7.9 to 157 W/mm^2. No spectral changes were observed before the Dz compound was added even at the highest laser power.

The light sensitivity was probed by lateral Raman mapping. We mapped the defect density in the entire area around the functionalization spot. After LAF (2 mW, 50× NA 0.55 objective, 2 h), a Raman mapping of the irradiated zone and its surroundings was performed with an Xplora Horiba spectrometer. The same excitation energy as for LAF (785 nm) was used, but an objective with higher magnification (×100, NA 0.9) was picked to obtain higher lateral resolution. At each *x*, *y* position we acquired a Raman spectrum containing the G and D modes. These modes were fitted with Lorentzian profiles, and the intensity (integrated peak

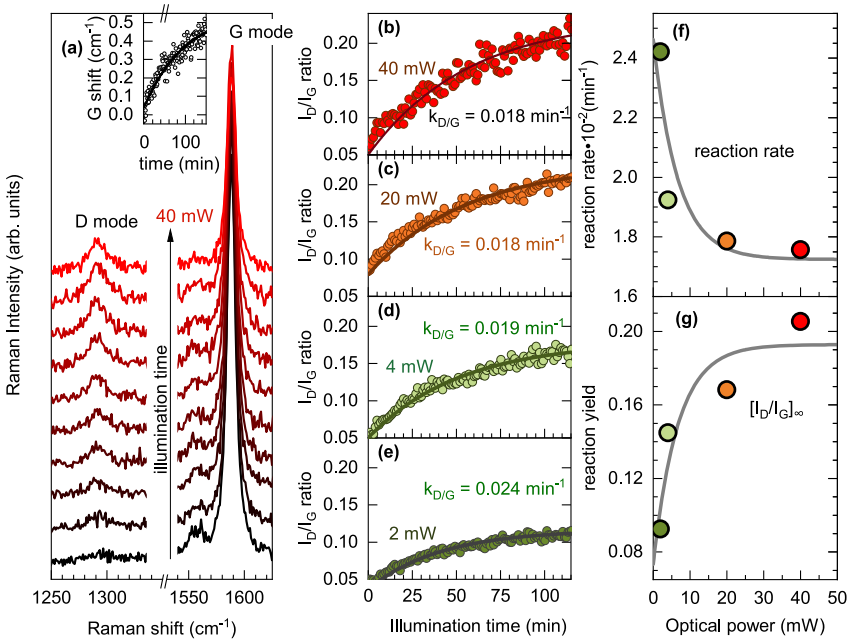

Figure 2. *In situ* control of the reaction kinetics via laser power. (a) Evolution of the Raman D and G modes during 40 mW 1.58 eV laser illumination, where time increases from the bottom to the top. The inset shows the time evolution of the G mode position. (b–e) I_D/I_G (integrated peak area ratio) over illumination time for 2, 4, 20, and 40 mW laser power. Symbols represent experimental data, and the line is a kinetic fit by eq 1. (f) Reaction rate and (g) reaction yield as a function of laser power. Symbols represent experimental data, and lines represent empirical expressions by eq 2.

area) of the D mode was divided by the intensity of the G^+ mode (LO phonon) shown in Figures 1b and 2d.

We probed chiral selectivity by comparing targeted and nontargeted species. We analyze the evolution of transition energies with resonant Raman spectroscopy. The RBMs were recorded before and after LAF (2 mW, 50× objective, 2 h) functionalization. A tunable excitation system was used with a Ti:sapphire laser (Coherent MBR 110) providing excitations from 700 to 1000 nm. The backscattered light was collected by a 50× objective before the functionalization and with an 100× objective after the functionalization to select nanotubes from the reaction center. A triple grating system of a T64000 Horiba spectrometer equipped with a 900 lines per mm grating and a silicon charge-coupled device was used to analyze the backscattered light. Raman shift and intensity were calibrated on a sulfur reference sample. Resonant Raman maps in Figure 4g,h were constructed from calibrated Raman spectral fits.

To demonstrate our technique we fabricated a single tube device and evaluated functionalization induced changes in its optical and electrical properties. Devices were prepared from commercial substrates (Active Business Company), which consist of a boron-doped silicon carrier wafer (resistance Ω < 0.005 cm) covered with 300 nm of thermal silicon oxide. The wafer was diced to 10 × 10 mm^2, and Pd electrodes with 500 nm gap size were defined by standard electron beam lithography. The toluene-based suspension containing a few chirality semiconducting nanotubes with diameters 1–1.2 nm, predominatly (9,7), (8,7), and (8,6), was used. Individual CNTs were deposited from solution onto multiple contact pairs by capacitive coupled ac dielectrophoresis.[31] The suspension was diluted to a concentration of 1 CNT/μm^3 solvent to deposit individual tubes, and a 20 μL droplet was placed onto the device array. A bias between 0.1 and 2 V at frequencies between 100 kHz and 1 MHz was applied between the common drain electrode and the back gate using an Agilent 33250 function generator. After 5 min the sample was rinsed with toluene to get rid of the excess polymer and annealed for 1.5 h at 160 °C to improve the contact conductivity. To confirm the deposition of individual CNTs, transport characteristics of the devices were measured at ambient conditions in a probe station with TRIAX probes using an Agilent 4155C semiconductor parameter analyzer. For current biasing, we have used for the source and the drain electrode separate source measurement units (SMUs) and operated the Agilent 4155C in constant current mode. The drain electrode has been set as a reference for the gate voltage which has been applied by a third SMU in constant voltage mode. A poly(methyl methacrylate) (PMMA) mask was deposited on top of device with a 50 nm window between the electrodes.

For applying our LAF method to our device, the substrate with the devices was covered with the DzBr solution for 45 min and irradiated with 785 nm at 40 mW and 5× magnification. The sample was then rinsed with water, blown dry with nitrogen, and annealed on a hot plate for 5 min at 130 °C.

Finally, with electroluminescence spectroscopy we studied the influence of the functionalization of the optical properties of the device. Samples were mounted on a custom-made sample holder, and chip contacts of up to eight devices were bonded onto palladium pads attached to this holder. *In situ* annealing at 60–70 °C was conducted via the integrated heater at a pressure below 10.6 mbar and the subsequent electroluminescence measurements were carried out without breaking vacuum. The cryostat has a 10 mm diameter optical access via a 0.5 mm thick quartz window, and the emitted light was collected with a Zeiss LD-Plan Neofluar objective (40×/0.6) of a customized Zeiss Axiotech Vario microscope and focused with an off-axis parabolic mirror (Thorlabs MPD149-P01, Ag, 25.4 mm, f/4) into an Acton SP-2360 (f/3.9) imaging spectrograph (Princeton Instruments) and dispersed via a 85

G/mm, 1.35 μm blazed grating onto an InGaAs photodiode linear array (PyLoN-IR Princeton Instruments) with 1024 pixels, sensitive from 950 to 1610 nm. The cryostat is positioned with sub-μm precision by a motorized *xy* scanning stage (8MTF, Standa), and the working distance between objective and sample surface is adjusted by a high precision objective piezoscanner (P-721 PIFOC/E-665 piezoamplifier, Physics Instruments), which allowed precise and stable positioning of the emitter. CNT devices mounted in the cryostat were driven by an Agilent 4155B semiconductor parameter analyzer. The noise in the spectra in Figure 5b was reduced by using a moving average of 15 periods, after performing all fitting operations.

RESULTS

Light Sensitivity. Kinetics. To begin, we investigate the light sensitivity of the reaction and study whether the functionalization can be controlled with light. We drop-casted a mixture of several semiconducting CNT chiralities onto the silicon substrate. After the CNTs adhered to the substrate, the sample was covered with water, as shown in Figure 1a. The laser light of 1.58 eV tuned in resonance with the second excitonic transition E_{22} of the (9,7) CNT was focused onto the nanotubes. The inelastically scattered light was instantly analyzed by a Raman spectrometer. A Raman spectrum after 1 min illumination is shown is Figure 1b. The highest peak at 1592 cm^{-1} is the G^+ mode due to the longitudinal vibration (we further omit the + symbol). The D mode near 1289 cm^{-1} is proportional to the sp^3 defect concentration in the CNT[21] and the ratio between the D and G modes scales with the defect density.[14] We started the laser-assisted functionalization (LAF) by adding 4-bromobenzenediazonium tetrafluoroborate (Dz-Br) to the solution (35 nmol/g). In 2 h the amount of defect centers produced by covalent functionalization increases yielding a more intense D mode; see inset in Figure 1b. The time evolution of the intensity ratios between the D and G modes is shown in Figure 1c and clearly reflects all the reaction details. The reference measurement is shown in Figure 1c by black symbols. We used the same experimental conditions without adding Dz-Br. No changes occurred in the Raman spectrum, indicating that in our setup the laser light does not perturb the CNTs in the absence of the reaction agent. While during intense laser illumination one could expect CNTs oxidation[32] or even defects healing,[33] these would only occur at higher laser densities[32] and dry conditions.

Through *in situ* functionalization we can follow real-time functionalization effects. The time evolution of the D and G modes during 2 hours illumination with 40 mW laser power is shown in Figure 2a. The I_D increases with time, reflecting the progress in reaction. At the same time, the G mode intensity shifts to higher energy; see inset in Figure 1a. The shift of 0.5 cm^{-1} is also accompanied by broadening, increasing full width at half maxima by 0.7 cm^{-1} as can be expected for doping induced effects.[25,34] The doping is a result of additional charge carriers shared by the functional moieties. For semiconducting CNTs the doping effects are relatively weak compared to the metallic ones. Moreover it scales nonlinearly with doping.[26,27] For monitoring the reaction kinetics the $\frac{I_D}{I_G}$ ratio is advantageous, since it has linear behavior with defect density and does not change upon doping.[26]

The reaction yield and product can be controlled with laser illumination power. We use the $\frac{I_D}{I_G}$ ratio for monitoring the reaction; shown in Figure 2b is the highest laser power used (40 mW). The D/G ratio increases from 0.07 to 0.2 within 120 min. By reduction of the laser power by 20 times (2 mW), the reaction kinetics is different; see Figure 2e. The D/G ratio increased only up to 0.1 within 120 min and is near at the saturation point, indicating lower reaction yield but higher reaction rate compared to the high laser power. The reaction kinetics for two intermediate steps for 4 and 20 mW is shown in Figure 2c and Figure 2d, respectively, each displaying slightly different kinetics. We quantify these changes by fitting the curves with the first-order differential equation:[35]

$$\frac{I_D}{I_G}(t) = \frac{I_D}{I_{G\infty}}\left(1 - e^{-k_D t}\right) + \frac{I_D}{I_{G0}} \quad (1)$$

where $\frac{I_D}{I_{G\infty}}$ and $\frac{I_D}{I_{G0}}$ reflect the defects density at infinite and zero reaction time, respectively. k_D is the reaction rate derived from the defect density. The experimental data are fitted by eq 1, and the fit is shown in Figure 2b–e by the solid lines. The parameters are listed in Table 1 along with the standard fit errors. The defects induced by the reaction can be associated with the reaction yield. The yield $\frac{I_D}{I_{G\infty}}$ increases with photon density and can be related to the variation of activation energy, which varies nonlinearly with optical power as shown in Figure 2g. This variation could in theory be induced by photogating of the nanotube on the SiO_2/Si surface, which is chirality independent.[36,37] We later perform the resonance Raman analysis to verify these effects. The positive effect of the light intensity on the reaction yield is comparable with the solution based studies.[16]

Table 1. Laser Power Control Parameters over the Diazonium/Nanotube Reaction Rate $k_D \pm 10^{-3}$ (min^{-1}) and Reaction Yield $\frac{I_D}{I_{G\infty}} \pm 5 \times 10^{-4}$ from Equation 1, Plotted in Figure 2

laser power (mW)	power density (W/mm^{-2})	k_D (min^{-1})	$\frac{I_D}{I_{G\infty}}$	D position (cm^{-1})	G fwhm (cm^{-1})
2	8	0.024	0.09	1288.8	8.6
4	16	0.019	0.14	1289.5	8.7
20	79	0.018	0.17	1291.5	9.3
40	158	0.018	0.21	1291.7	9.4

The reaction rate displays a curious behavior decreasing with laser power, as shown in Figure 2e. We can use this dependence to better understand the reaction mechanism. In order for reaction to occur, a free aryl radical must be created first.[38] There are two possibilities to generate a radical: (I) to generate the radical via the direct electron extraction from CNT[39] and (II) that works through the interaction of the radical with the base,[40,41] resulting in an diazonium anhydride intermediate species. This species can be thermally decomposed into the aryl radical. While the II mechanism was generally accepted, recent experiments show that the reaction can occur without a base, when illuminated by light, pointing rather to the I pathway. That mechanism will require photoexcitation of the nanotube, which is more efficient near its absorption bands (E_{ii} energies). This is in line with solution-based chiral selectivity studies ascribe.[16] In both I and II pathways the reaction rate must increase with higher laser power, due to more efficient heating induced diffusion or

photoexcitation.[42] Instead we find that the reaction is slower for higher laser powers; see Figure 2f. We attribute this counterintuitive behavior to a competing parallel reaction. As is commonly known, the diazonium cations decompose in water into nitrogen and phenyl when enough thermal energy is given to the system.[43] Higher laser energy induces more local heat development, thus accelerating the competing reaction[43] that effectively reduces the production of the aryl radicals. The heat is instantly carried away from the nanotube surface as no heat-induced effects are observed in the Raman spectrum during reference measurements shown in Figure 1c. The competing reaction leads to a retardation of the functionalization due to a reduced concentration of reactant around the nanotube surface.

We find that the reaction rate k and the reaction yield $C\left(\frac{I_D}{I_G}_\infty\right)$ from eq 1 dependence on laser power follow the empirical expression

$$k(P),\ C(P) = A_{k,C} + B_{k,C}(1 + e^{-k_p P}) \quad (2)$$

with A, B, and k_p as constants ($A_k = 7 \times 10^{-3}$ min^{-1}, $A_C = 0.1$ min^{-1}, $B_k = 0.01$ min^{-1}, $B_C = 7 \times 10^{-2}$ min^{-1}, and $k_p = 1.5 \times 10^{-2}$ mW^{-1}). The plots of eq 2 with these parameters are shown in Figure 2e by full lines. They may be equally applicable for substrate supported nanotubes as well as for bulk solutions with low opacity, enabling propagation of the activation light through the entire volume. Two control parameters can be used to achieve the desired functionalization rate: the photon density and the illumination time. When a fast reaction is desired, the highest laser power should be applied. Up to now we investigated the CNTs under the laser spot; we also need to check them in the dark areas.

We probed light sensitivity of the reaction by spatial Raman mapping. After the LAF, we rinsed the sample with water multiple times and dried it. We collected Raman spectra in the area around the functionalization spot (FS) using a higher lateral resolution of 600 nm, as shown in Figure 3. At each lateral position we evaluated the ratio between the D and G modes and assessed the functionalization degree. The D/G ratio is plotted as a two-dimensional Raman map in Figure 3b. The highest degree of functionalization (D/G = 0.4) is observed in the middle of the FS compared to the unperturbed nanotubes outside the FS (D/G = 0.1). We estimate the functional groups concentration in the middle to be equivalent to ~1:150 of molar [Dz]/[C] ratios, sufficient to produce emission from defect states.[5] Figure 3a details the characteristic D and G$^+$ Raman modes of semiconducting nanotubes at ~1289 and 1592 cm^{-1}, respectively, at three different distances from the focus center.[1] The doping effects scale together with defect concentration, which can be best estimated by the D mode position.[27,44] The D mode shifts by 1.1 cm^{-1} to higher energies between the edge and the middle of FS, indicating the p-doping type.[27,44]

The increase of the defect density within the functionalization spot indicates a successful laser assisted reaction. The defect density inside the focus increases from the edges to the middle as shown by the line profile of the D/G ratio in Figure 3c. The defect density follows the Gaussian intensity profile of the laser beam. The full width at half-maximum of the profile of 2.2 μm coincides with the width of the laser spot. It suggests that the reaction yield is proportional to the photon flux density (laser power), and functionalization gradients can be

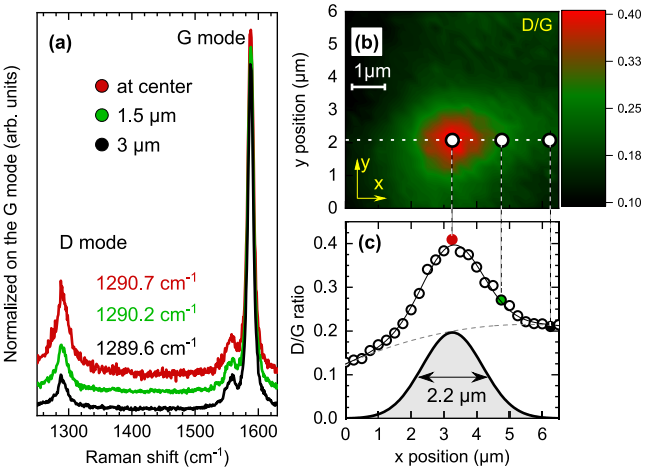

Figure 3. Light sensitivity of the reaction. (a) Raman spectra acquired at different distances from the functionalization spot center excited at 1.58 eV. (b) Lateral variation of the intensity ratio between the D and G Raman modes over the functionalization spot. Horizontal dashed line indicates where the linear profile is shown in (c). (c) D−G profile as a function of the x position. Symbols represent experimental points, and the line is a fit by Gaussian line shape. The width of the Gaussian peak corresponds to the full width at half-maximum of the laser spot.

generated by laser light. The above experiments were performed at the same excitation energy as activation energy (1.58 eV), thus reporting the effects in (9,7) nanotube. Now we turn to the analysis of other chiralities.

Chiral Selectivity. Transition Energies Shifts Investigated with Resonance Raman Spectroscopy. The G and D modes have for all nanotubes similar vibrational energies and are both excited in a broad excitation window of 190 meV, making it impossible to distinguish between chiralities present in the sample. The energies of the radial breathing modes (RBMs) on the other hand depend on tube diameter.[45] We apply resonant Raman spectroscopy to RBMs to access transition energies of each species. Raman spectra in the low energy region at three excitation energies are shown in Figure 4a−c. The modes are index identified as (8,6) 247.6 cm^{-1}, (8,7) 232.5 cm^{-1}, and (9,7) 219.5 cm^{-1}.[45] We measured the intensity of each mode as a function of laser excitation energies; see Figure 4d−f. These Raman profiles are described by the third-order perturbation theory:[45,46]

$$I_{\text{Raman}}(E_{\text{las}}) = E_{\text{las}}^4 \left[\frac{M_{\text{exc-ph}}^2 M_{\text{exc-RBM}}}{(E_{\text{las}} - E_{22} - i\gamma)(E_{\text{las}} - \hbar\omega_{\text{RBM}} - E_{22} - i\gamma)} \right]^2 \quad (3)$$

where M_c is the matrix element combining exciton−photon and exciton−phonon coupling. E_{22} is the energy of the second excitonic state, and γ is the broadening factor related to the finite lifetime of the exciton. The nonresonant E_{las}^4 dependence in eq 3 is eliminated by calibration on the Raman reference sample. The fits are shown by the solid lines in Figure 4d−f, and the parameters are listed in Table 2. The transition energies of the pristine and functionalized (9,7) CNT (vertical lines) differ by 10 meV, whereas the transition energies of the (8,6) and (8,7) CNTs remain constant. The difference in transition energies can be also viewed on resonance Raman maps; see Figure 4g,h. The vertical axis represents the laser

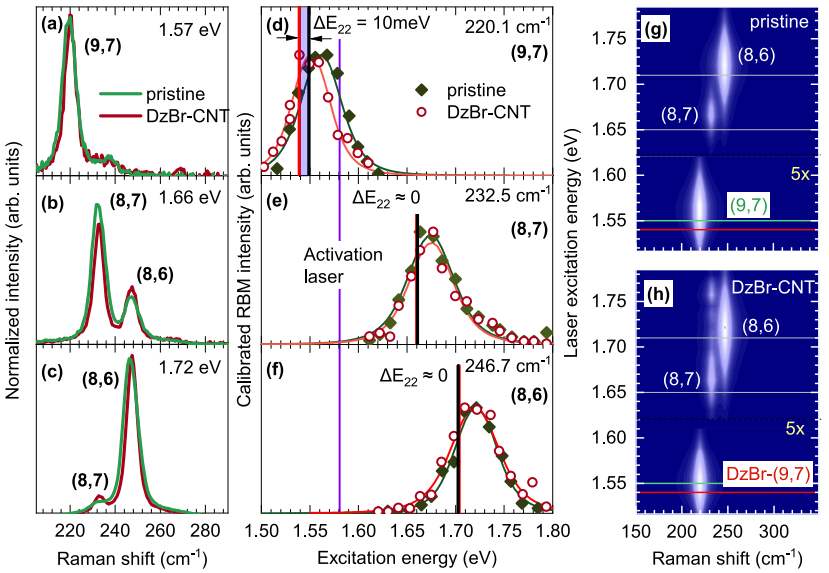

Figure 4. Chiral selectivity of the reaction. Radial breathing modes before (green) and after (red) functionalization excited at three different wavelengths (a) 1.57 eV, (b) 1.66 eV, and (c) 1.72 eV. Intensities of the RBMs as a function of excitation energy shown in (d), (e), and (f) for (9,7), (8,7), and (8,6) nanotubes, respectively. The symbols represent the experimental data before (green) and after (red) functionalization. Symbols represent experimental data, and lines are the fits with eq 3. Vertical colored lines mark the E_{22} transition energies. The vertical purple line indicates the laser energy E_f = 1.58 eV used to drive the functionalization. Resonant Raman maps of (g) pristine and (h) DzBr-CNTs with indicated chiralities and transition energies marked by horizontal lines.

Table 2. Second Transition Energy E_{22} for Pristine Nanotubes (prist) and DzBr-CNT (func) Acquired by Fitting the Resonance Raman Profiles in Figure 4a–c[a]

(n,m)	RBM position (cm^{-1})	detuning (meV)	E_{22}^{prist} (eV)	E_{22}^{func} (eV)	E_{22} shift (meV)	γ_{prist} (meV)	γ_{func} (meV)
(8,6)	248	84	1.65	1.65	−0.7	32	37
(8,7)	233	136	1.71	1.71	0.8	31	39
(9,7)	220	−22	1.55	1.54	−10.5	32	28

[a]Detuning is $E_{22} - E_f$ (E_f = 1.58 eV), and E_{22} shift = $E_{22}^{func} - E_{22}^{prist}$. The average E_{22} (γ) error is ±1.5 (3.5) meV.

excitation energy and horizontal Raman shift, and the blue (red) color represents low (high) Raman intensity. The vertical positions of the resonant peaks are different for the DzBr (9,7) and (9,7) (see horizontal lines in Figure 4g,f), whereas the positions of the (8,6) and (8,7) do not change after functionalization.

We attribute the shift of transition energies to the dielectric effects. During covalent functionalization the functional groups either directly influence the exciton screening or indirectly change the polymer wrapping. A denser dielectric environment leads to a red-shift of the optical transition energies.[47−49] The shifts of transition energies are broadly used to confirm covalent and noncovalent functionalization.[34,50] But the increase of the D mode (Figure 2a) unambiguously indicates covalent type and the E_{ii} shift may serve as an additional effect indicating functionalization. Nontargeted species (8,6) and (8,7) do not display any shift of transition energy but might still be functionalized to some degree, certainly weaker compared to the targeted (9,7) species; see Figure 4.

We suggest the photoexcitation of charge carriers to be responsible for the chiral selectivity mechanism. While the

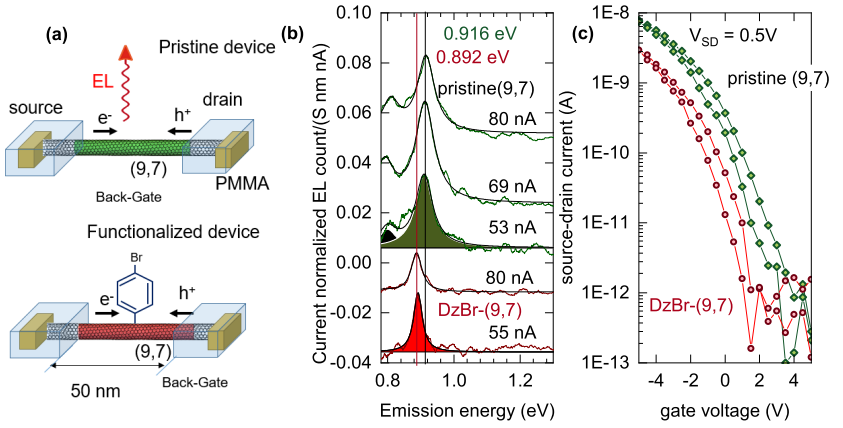

Figure 5. Aryl bromide functionalization of an electroluminescent (9,7) nanotube device. (a) Device sketch and geometry. (b) Electroluminescence spectra of (9,7) nanotubes at different currents before functionalization (green) and after functionalization (red). Peaks were fitted by a single Lorentzian (see filled peaks). (c) Transconductance curves measured before and after functionalization.

local thermal activation mechanism[16] would yield similar effects, it is not compatible with base-free reactions[20] and might be less chirality selective, since the heat is quickly distributed within the bundle. In direct photoexcitation the laser generates excitons that partly relax into charge carriers. These charge carriers participate in the aryl radical formation,[39] yielding higher reactivity of photoexcited CNTs. With this interpretation we conclude that the reaction yield is proportional to the absorption overlay with the laser energy; i.e., an additional activation occurs if E_f is in the range $(E_{22} - \gamma/2, E_{22} + \gamma/2)$, where γ is obtained from Raman profiles; see Table 2. The overlap of energies can be directly seen by the relative energies of the RBM resonance Raman profiles and E_f in Figure 4d–f. Charge carriers could be also generated by the Si/SiO_2 interface, but this effect appears to be less important. It should equally affect all chiralities, whereas we observe pronounced chiral selectivity in Figure 4. The chiral selectivity of the reaction is demonstrated here between Dz-Br and (9,7) nanotubes; however, we anticipate that method to be applicable to any arbitrary (n,m) chirality and diazonium compound. Finally, we further test our aryl bromide functionalization on individual nanotube preintegrated into a device.

Device Integration and Electroluminescence. Now we discuss the application of the LAF method to a CNT device. A sketch of the device is shown in Figure 5a, where a nanotube is positioned between two electrodes by dielectrophoresis; see methods section. An equal amount of holes and electrons is injected through opposite electrodes, followed by recombination in the middle and emerging photoluminescence.[28,51] A spectrum of emitted light from such a device prior to functionalization is shown in Figure 5b (green trace). The peaks around 0.9 and 0.8 eV are associated with the emission from an E_{11} exciton (electron–hole pair)[52] and a trion (charged exciton) of the (9,7) E_{11} state, as discussed by Gaulke et al.[28] The absence of other peaks indicates that this device most likely comprises only a single nanotube. The position of the E_{11} emission varies by up to 3 meV when driven at different DC currents.

As a next step we performed the LAF directly on the device. In order to ensure that the aryl ring binds the nanotube in the middle, we applied a PMMA mask with a 50 nm slit centered between the two electrodes; see methods section. The emission of the 4-bromophenyl functionalized device was collected for a series of currents as shown in Figure 5b by the red color. The emission of the ground E_{11} excitonic state is found at 0.92 eV, which is red-shifted by approximately 20 meV compared to the emission of the pristine device. The shift of transition energy indicates successful functionalization. We observed a similar effect in the E_{22} transition by resonance Raman spectroscopy; see Figure 4. On the other hand, the shift correlates with a D to G intensity ratio of at least 0.2 (Figure 2a,d) and indicates that covalent bonds for brightening of the dark emission states have been formed.[5] The emission of the defect state is known to be 180 meV below the E_{11} ground excitonic bright state and is expected at 0.73 eV[5] and is outside of our detection range.

Aryl bromide functionalization changes the doping level of the nanotubes. This manifests in a suppression of the (9,7) trion (charged exciton) at 0.8 eV emission. However, this effect is stronger than expected; additionally, the E_{11} trion might be suppressed by the defect formation, as reported for two-dimensional excitons.[53] Further, the Fermi level shift can be seen in the transconductance curves, shown in Figure 5c. The p-type conductance is typical for CNTs in contact with Pd electrodes mounted onto SiO_2/Si surfaces due to the Schottky barrier for holes being smaller than for electrons. The positive threshold voltage for current switching indicates initial p-doping of the device which reduces to lower gate voltages after functionalization. Only from transport data we cannot rule out nonfunctionalization related doping origins, such as filling and depletion of trapped states. But in the Raman analysis we find similar effects where a broadening and shift of the G and D modes were observed. Thus, the functionalization of semiconducting CNTs is detectable in electrical transport data, as have been previously reported for metallic nanotubes.[54,55] The on/off currents of our device do not change much; see Figure 5c. We conclude that the covalent functionalization is not sufficient to hinder the conductance of semiconducting CNTs, in contrast to the metallic ones.[56]

The origin of the red-shift of the second excitonic state (obtained via Raman excitation mapping) and the first excitonic state (obtained by EL spectroscopy) could be induced by the dielectric screening of the excitons.[49] The screening might be provided by the aryl rings covering the nanotube surface. An alternative physical effect providing the shift of excitonic levels can be strain;[25,34] however, strain along the nanotube axis causes shifts of the second (E_{22}) and first states (E_{11}) in opposite directions,[57] which is not the case in our system. Therefore, dielectric screening appears to be the dominant mechanism influencing optical properties of functionalized CNTs. Note that the lateral control of the reaction center was improved past the diffraction limit[20] by applying polymer masks and electron beam lithography. The next step is the functionalization of devices built upon small diameter enriched semiconducting nanotubes,[58,59] where the defect PL is better detectable. Furthermore, the on-device functionalization scheme can be of use for other sp^2 hybridized nanocarbons with optical transitions in the visible wavelength range such as twisted graphene layers, graphene nanoribbons, and graphene quantum dots.[60−62]

CONCLUSIONS

A novel method that enables a local and chirality-selective covalent functionalization of nanotubes on surfaces and in devices was successfully demonstrated. Laser assisted functionalization of (9,7) nanotube with 4-bromophenyl was studied by spatial Raman mapping of defect density, which confirmed the light sensitivity of the reaction. The nanotubes inside the illumination spot were functionalized, whereas the non-illuminated areas remained unperturbed. The influence of the photon flux density on reaction kinetics was explored by *in situ* reaction monitoring. The reaction product increased and reaction rate decreased with laser power. The drop of reaction rate with the increase of photon flux reveals a competing mechanism and could be due to diazonium salt decomposition activated by local heat. We proposed empirical expressions for controlling the reaction kinetics applicable both to the processes on the surface and in solutions with low opacity.

To test chiral selectivity of the reaction, we compared E_{22} transition energies of the pristine and functionalized nanotubes before and after functionalization. The transition energies were determined by resonant Raman spectroscopy. The E_{22} of (9,7) nanotube red-shifted by 10 meV in contrast with E_{22} of the (8,6) and (8,7) retaining their positions. These two chiralities were out of resonance with the laser energy during

functionalization. Chiral selectivity was achieved by matching the laser light energy with the optical transition of the (9,7) nanotube only.

We applied the laser-assisted aryl bromide functionalization to an electroluminescent device made of (9,7) nanotube. The reaction center was controlled beyond the diffraction limit by a 50 nm opened PMMA slit mark. The functionalization yielded a 25 meV red-shift of the ground optical state (E_{11}) electroluminescence. A red shift of the first (EL) and the second (resonance Raman) transitions shows evidence of dielectric screening of the exciton wave function by molecules. The transport characteristics of the functionalized device and Raman analysis suggest a doping effect provided by the functional group. We therefore conclude that laser-assisted on-device covalent functionalization opens a route toward nanoscale engineering of trapped excitonic states for optoelectronic circuits.

AUTHOR INFORMATION

Corresponding Authors

Georgy Gordeev − *Department of Physics, Freie Universität Berlin, 14195 Berlin, Germany; Department of Physics and Materials Science, University of Luxembourg, L-4422 Belvaux, Luxembourg;* orcid.org/0000-0002-3273-2105; Email: gordeev@zedat.fu-berlin.de

Ralph Krupke − *Institute of Nanotechnology and Institute of Quantum Materials and Technologies, Karlsruhe Institute of Technology, 76021 Karlsruhe, Germany; Institute of Materials Science, Technische Universität Darmstadt, 64287 Darmstadt, Germany;* orcid.org/0000-0001-8427-8592; Email: ralph.krupke@kit.edu

Authors

Thomas Rosenkranz − *Institute of Nanotechnology, Karlsruhe Institute of Technology, 76021 Karlsruhe, Germany; Institute of Materials Science, Technische Universität Darmstadt, 64287 Darmstadt, Germany*

Frank Hennrich − *Institute of Nanotechnology and Institute of Quantum Materials and Technologies, Karlsruhe Institute of Technology, 76021 Karlsruhe, Germany*

Stephanie Reich − *Department of Physics, Freie Universität Berlin, 14195 Berlin, Germany;* orcid.org/0000-0002-2391-0256

Author Contributions

# G.G. and T.R. contributed equally.

Notes

The authors declare no competing financial interest.

ACKNOWLEDGMENTS

G.G. and S.R. acknowledge Focus Area NanoScale of Freie Universitaet Berlin. S.R. acknowledges support by the Deutsche Forschungsgemeinschaft under Grant SPP 2244 and the German Research Foundation (DFG via Grant SFB 658, Subproject A6). We thank Oisín Garrity for language checkup. F.H. and R.K. acknowledge support by the Helmholtz Association and the Volkswagen Foundation.

REFERENCES

(1) Thomsen, C.; Reich, S. Raman Scattering in Carbon Nanotubes. In *Light Scattering in Solids IX*; Manuel, C., Merlin, R., Eds.; Springer: Berlin, 2007; pp 164−169.

(2) He, X.; Htoon, H.; Doorn, S. K.; Pernice, W. H.; Pyatkov, F.; Krupke, R.; Jeantet, A.; Chassagneux, Y.; Voisin, C. Carbon nanotubes as emerging quantum-light sources. *Nat. Mater.* **2018**, *17*, 663−670.

(3) Sun, Y. P.; Fu, K.; Lin, Y.; Huang, W. Functionalized carbon nanotubes: Properties and applications. *Acc. Chem. Res.* **2002**, *35*, 1096−1104.

(4) Ernst, F.; Heek, T.; Setaro, A.; Haag, R.; Reich, S. Energy transfer in nanotube-perylene complexes. *Adv. Funct. Mater.* **2012**, *22*, 3921−3926.

(5) Piao, Y.; Meany, B.; Powell, L. R.; Valley, N.; Kwon, H.; Schatz, G. C.; Wang, Y. Brightening of carbon nanotube photoluminescence through the incorporation of sp 3 defects. *Nat. Chem.* **2013**, *5*, 840−845.

(6) He, X.; Sun, L.; Gifford, B. J.; Tretiak, S.; Piryatinski, A.; Li, X.; Htoon, H.; Doorn, S. K. Intrinsic limits of defect-state photoluminescence dynamics in functionalized carbon nanotubes. *Nanoscale* **2019**, *11*, 9125−9132.

(7) Kwon, H.; Furmanchuk, A.; Kim, M.; Meany, B.; Guo, Y.; Schatz, G. C.; Wang, Y. Molecularly Tunable Fluorescent Quantum Defects. *J. Am. Chem. Soc.* **2016**, *138*, 6878−6885.

(8) Ma, X.; Adamska, L.; Yamaguchi, H.; Yalcin, S. E.; Tretiak, S.; Doorn, S. K.; Htoon, H. Electronic structure and chemical nature of oxygen dopant states in carbon nanotubes. *ACS Nano* **2014**, *8*, 10782−10789.

(9) Luo, Y.; Ahmadi, E. D.; Shayan, K.; Ma, Y.; Mistry, K. S.; Zhang, C.; Hone, J.; Blackburn, J. L.; Strauf, S. Purcell-enhanced quantum yield from carbon nanotube excitons coupled to plasmonic nanocavities. *Nat. Commun.* **2017**, *8*, 1413.

(10) Mueller, T.; Kinoshita, M.; Steiner, M.; Perebeinos, V.; Bol, A. A.; Farmer, D. B.; Avouris, P. Efficient narrow-band light emission from a single carbon nanotube p-n diode. *Nat. Nanotechnol.* **2010**, *5*, 27−31.

(11) Khasminskaya, S.; Pyatkov, F.; Słowik, K.; Ferrari, S.; Kahl, O.; Kovalyuk, V.; Rath, P.; Vetter, A.; Hennrich, F.; Kappes, M. M.; et al. Fully integrated quantum photonic circuit with an electrically driven light source. *Nat. Photonics* **2016**, *10*, 727−732.

(12) Strano, M. S.; Dyke, C. A.; Usrey, M. L.; Barone, P. W.; Allen, M. J.; Shan, H.; Kittrell, C.; Hauge, R. H.; Tour, J. M.; Smalley, R. E. Electronic structure control of single-waited carbon nanotube functionalization. *Science* **2003**, *301*, 1519−1522.

(13) Usrey, M. L.; Lippmann, E. S.; Strano, M. S. Evidence for a two-step mechanism in electronically selective single-walled carbon nanotube reactions. *J. Am. Chem. Soc.* **2005**, *127*, 16129−16135.

(14) Mohamed, A. A.; Salmi, Z.; Dahoumane, S. A.; Mekki, A.; Carbonnier, B.; Chehimi, M. M. Functionalization of nanomaterials with aryldiazonium salts. *Adv. Colloid Interface Sci.* **2015**, *225*, 16−36.

(15) Saha, A.; Gifford, B. J.; He, X.; Ao, G.; Zheng, M.; Kataura, H.; Htoon, H.; Kilina, S.; Tretiak, S.; Doorn, S. K. Narrow-band single-photon emission through selective aryl functionalization of zigzag carbon nanotubes. *Nat. Chem.* **2018**, *10*, 1089−1095.

(16) Powell, L. R.; Piao, Y.; Wang, Y. Optical Excitation of Carbon Nanotubes Drives Localized Diazonium Reactions. *J. Phys. Chem. Lett.* **2016**, *7*, 3690−3694.

(17) Powell, L. R.; Kim, M.; Wang, Y. Chirality-Selective Functionalization of Semiconducting Carbon Nanotubes with a Reactivity-Switchable Molecule. *J. Am. Chem. Soc.* **2017**, *139*, 12533−12540.

(18) Kim, W. J.; Usrey, M. L.; Strano, M. S. Selective functionalization and free solution electrophoresis of single-walled carbon nanotubes: Separate enrichment of metallic and semiconducting SWNT. *Chem. Mater.* **2007**, *19*, 1571−1576.

(19) Berger, F. J.; Lüttgens, J.; Nowack, T.; Kutsch, T.; Lindenthal, S.; Kistner, L.; Müller, C. C.; Bongartz, L. M.; Lumsargis, V. A.; Zakharko, Y.; et al. Brightening of Long, Polymer-Wrapped Carbon

Nanotubes by sp3 Functionalization in Organic Solvents. *ACS Nano* **2019**, *13*, 9259−9269.
(20) Huang, Z.; Powell, L. R.; Wu, X.; Kim, M.; Qu, H.; Wang, P.; Fortner, J. L.; Xu, B.; Ng, A. L.; Wang, Y. H. Photolithographic Patterning of Organic Color-Centers. *Adv. Mater.* **2020**, *32*, 1906517.
(21) Maultzsch, J.; Reich, S.; Thomsen, C. Chirality-selective Raman scattering of the D mode in carbon nanotubes. *Phys. Rev. B* **2001**, *64*, 121407.
(22) Thomsen, C.; Reich, S. Double resonant raman scattering in graphite. *Phys. Rev. Lett.* **2000**, *85*, 5214−5217.
(23) Cançado, L. G.; Jorio, A.; Ferreira, E. H.; Stavale, F.; Achete, C. A.; Capaz, R. B.; Moutinho, M. V.; Lombardo, A.; Kulmala, T. S.; Ferrari, A. C. Quantifying defects in graphene via Raman spectroscopy at different excitation energies. *Nano Lett.* **2011**, *11*, 3190−3196.
(24) Cançado, L. G.; Da Silva, M. G.; Martins Ferreira, E. H.; Hof, F.; Kampioti, K.; Huang, K.; Pénicaud, A.; Achete, C. A.; Capaz, R. B.; Jorio, A. Disentangling contributions of point and line defects in the Raman spectra of graphene-related materials. *2D Mater.* **2017**, *4*, 025039.
(25) Gordeev, G.; Setaro, A.; Glaeske, M.; Jürgensen, S.; Reich, S. Doping in covalently functionalized carbon nanotubes: A Raman scattering study. *Physica Status Solidi (B)* **2016**, *253*, 2461−2467.
(26) Grimm, S.; Schießl, S. P.; Zakharko, Y.; Rother, M.; Brohmann, M.; Zaumseil, J. Doping-dependent G-mode shifts of small diameter semiconducting single-walled carbon nanotubes. *Carbon* **2017**, *118*, 261−267.
(27) Das, A.; Sood, A. K. Renormalization of the phonon spectrum in semiconducting single-walled carbon nanotubes studied by Raman spectroscopy. *Phys. Rev. B* **2009**, *79*, 235429.
(28) Gaulke, M.; Janissek, A.; Peyyety, N. A.; Alamgir, I.; Riaz, A.; Dehm, S.; Li, H.; Lemmer, U.; Flavel, B. S.; Kappes, M. M.; et al. Low temperature Electroluminescence Excitation Mapping of Excitons and Trions in Short-Channel Monochiral Carbon Nanotube Devices. *ACS Nano* **2020**, *14*, 2709−2717.
(29) Stürzl, N.; Hennrich, F.; Lebedkin, S.; Kappes, M. M. Near monochiral single-walled carbon nanotube dispersions in organic solvents. *J. Phys. Chem. C* **2009**, *113*, 14628−14632.
(30) Hennrich, F.; Li, W.; Fischer, R.; Lebedkin, S.; Krupke, R.; Kappes, M. M. Length-Sorted, Large-Diameter, Polyfluorene-Wrapped Semiconducting Single-Walled Carbon Nanotubes for High-Density, Short-Channel Transistors. *ACS Nano* **2016**, *10*, 1888−1895.
(31) Vijayaraghavan, A.; Blatt, S.; Weissenberger, D.; Oron-Carl, M.; Hennrich, F.; Gerthsen, D.; Hahn, H.; Krupke, R. Ultra-large-scale directed assembly of single-walled carbon nanotube devices. *Nano Lett.* **2007**, *7*, 1556−1560.
(32) Tachibana, M. Characterization of Laser-Induced Defects and Modification in Carbon Nanotubes by Raman Spectroscopy. In *Physical and Chemical Properties of Carbon Nanotubes*; Suzuki, S., Ed.; InTech: Rijeka, Croatia, 2013.
(33) Van, H. H.; Badura, K.; Liang, R.; Okoli, O.; Zhang, M. Laser-induced graphitic healing of carbon nanotubes aligned in a sheet. *Journal of Laser Applications* **2017**, *29*, 022010.
(34) Setaro, A.; Adeli, M.; Glaeske, M.; Przyrembel, D.; Bisswanger, T.; Gordeev, G.; Maschietto, F.; Faghani, A.; Paulus, B.; Weinelt, M.; et al. Preserving π-conjugation in covalently functionalized carbon nanotubes for optoelectronic applications. *Nat. Commun.* **2017**, *8*, 14281.
(35) Connors, A. K. *Chemical Kinetics: The Study of Reaction Rates in Solution*; John Wiley & Sons: New York, 1990; Vol. *180*, p 140.
(36) Benfante, A.; Giambra, M. A.; Pernice, R.; Stivala, S.; Calandra, E.; Parisi, A.; Cino, A. C.; Dehm, S.; Danneau, R.; Krupke, R.; et al. Employing Microwave Graphene Field Effect Transistors for Infrared Radiation Detection. *IEEE Photonics J.* **2018**, *10*, 6801407.
(37) Riaz, A.; Alam, A.; Selvasundaram, P. B.; Dehm, S.; Hennrich, F.; Kappes, M. M.; Krupke, R. Near-Infrared Photoresponse of Waveguide-Integrated Carbon Nanotube-Silicon Junctions. *Advanced Electronic Materials* **2019**, *5*, 1800265.
(38) Schmidt, G.; Gallon, S.; Esnouf, S.; Bourgoin, J. P.; Chenevier, P. Mechanism of the coupling of diazonium to single-walled carbon nanotubes and its consequences. *Chem.—Eur. J.* **2009**, *15*, 2101−2110.
(39) Dyke, C. A.; Stewart, M. P.; Maya, F.; Tour, J. M. Diazonium-Based Functionalization of Carbon Nanotubes: XPS and GC-MS Analysis and Mechanistic Implications. *Synlett* **2004**, 155−160.
(40) Galli, C. Radical Reactions of Arenediazonium Ions: An Easy Entry into the Chemistry of the Aryl Radical. *Chem. Rev.* **1988**, *88*, 765−792.
(41) Gomberg, M.; Bachmann, W. E. The synthesis of biaryl compounds by means of the diazo reaction. *J. Am. Chem. Soc.* **1924**, *46*, 2339−2343.
(42) Burek, B. O.; Bahnemann, D. W.; Bloh, J. Z. Modeling and Optimization of the Photocatalytic Reduction of Molecular Oxygen to Hydrogen Peroxide over Titanium Dioxide. *ACS Catal.* **2019**, *9*, 25−37.
(43) DeTar, D. L. F.; Ray Ballentine, A. The Mechanisms of Diazonium Salt Reactions. II. A Redetermination of the Rates of the Thermal Decomposition of Six Diazonium Salts in Aqueous Solution. *J. Am. Chem. Soc.* **1956**, *78*, 3916−3920.
(44) Hatting, B.; Heeg, S.; Ataka, K.; Heberle, J.; Hennrich, F.; Kappes, M. M.; Krupke, R.; Reich, S. Fermi energy shift in deposited metallic nanotubes: A Raman scattering study. *Phys. Rev. B* **2013**, *87*, 165442.
(45) Maultzsch, J.; Telg, H.; Reich, S.; Thomsen, C. Radial breathing mode of single-walled carbon nanotubes: Optical transition energies and chiral-index assignment. *Phys. Rev. B* **2005**, *72*, 205438.
(46) Gordeev, G.; Jorio, A.; Kusch, P.; Vieira, B. G.; Flavel, B.; Krupke, R.; Barros, E. B.; Reich, S. Resonant anti-Stokes Raman scattering in single-walled carbon nanotubes. *Phys. Rev. B* **2017**, *96*, 245415.
(47) Perebeinos, V.; Tersoff, J.; Avouris, P. Scaling of excitons in carbon nanotubes. *Phys. Rev. Lett.* **2004**, *92*, 257402.
(48) Walsh, A. G.; Vamivakas, A. N.; Yin, Y.; Cronin, S. B.; Ünlü, M. S.; Goldberg, B. B.; Swan, A. K. Screening of excitons in single, suspended carbon nanotubes. *Nano Lett.* **2007**, *7*, 1485−1488.
(49) Araujo, P. T.; Jorio, A.; Dresselhaus, M. S.; Sato, K.; Saito, R. Diameter dependence of the dielectric constant for the excitonic transition energy of single-wall carbon nanotubes. *Phys. Rev. Lett.* **2009**, *103*, 146802.
(50) Roquelet, C.; Lauret, J. S.; Alain-Rizzo, V.; Voisin, C.; Fleurier, R.; Delarue, M.; Garrot, D.; Loiseau, A.; Roussignol, P.; Delaire, J. A.; et al. Π-Stacking functionalization of carbon nanotubes through micelle swelling. *ChemPhysChem* **2010**, *11*, 1667−1672.
(51) Marquardt, C. W.; Grunder, S.; Błaszczyk, A.; Dehm, S.; Hennrich, F.; Löhneysen, H. V.; Mayor, M.; Krupke, R. Electroluminescence from a single nanotube-molecule-nanotube junction. *Nat. Nanotechnol.* **2010**, *5*, 863−867.
(52) Bachilo, S. M.; Strano, M. S.; Kittrell, C.; Hauge, R. H.; Smalley, R. E.; Weisman, R. B. Structure-assigned optical spectra of single-walled carbon nanotubes. *Science* **2002**, *298*, 2361−2366.
(53) Greben, K.; Arora, S.; Harats, M. G.; Bolotin, K. I. Intrinsic and Extrinsic Defect-Related Excitons in TMDCs. *Nano Lett.* **2020**, *20*, 2544−2550.
(54) Wilson, H.; Ripp, S.; Prisbrey, L.; Brown, M. A.; Sharf, T.; Myles, D. J.; Blank, K. G.; Minot, E. D. Electrical monitoring of sp3 defect formation in individual carbon nanotubes. *J. Phys. Chem. C* **2016**, *120*, 1971−1976.
(55) Lee, Y.; Trocchia, S. M.; Warren, S. B.; Young, E. F.; Vernick, S.; Shepard, K. L. Electrically Controllable Single-Point Covalent Functionalization of Spin-Cast Carbon-Nanotube Field-Effect Transistor Arrays. *ACS Nano* **2018**, *12*, 9922−9930.
(56) Goldsmith, B. R.; Coroneus, J. G.; Khalap, V. R.; Kane, A. A.; Weiss, G. A.; Collins, P. G. Conductance-controlled point functionalization of single-walled carbon nanotubes. *Science* **2007**, *315*, 77−81.
(57) Berger, S.; Iglesias, F.; Bonnet, P.; Voisin, C.; Cassabois, G.; Lauret, J. S.; Delalande, C.; Roussignol, P. Optical properties of

carbon nanotubes in a composite material: The role of dielectric screening and thermal expansion. *J. Appl. Phys.* **2009**, *105*, 094323.
(58) Li, H.; Gordeev, G.; Garrity, O.; Reich, S.; Flavel, B. S. Separation of Small-Diameter Single-Walled Carbon Nanotubes in One to Three Steps with Aqueous Two-Phase Extraction. *ACS Nano* **2019**, *13*, 2567−2578.
(59) Graf, A.; Zakharko, Y.; Schießl, S. P.; Backes, C.; Pfohl, M.; Flavel, B. S.; Zaumseil, J. Large scale, selective dispersion of long single-walled carbon nanotubes with high photoluminescence quantum yield by shear force mixing. *Carbon* **2016**, *105*, 593−599.
(60) Denk, R.; Hohage, M.; Zeppenfeld, P.; Cai, J.; Pignedoli, C. A.; Söde, H.; Fasel, R.; Feng, X.; Müllen, K.; Wang, S.; et al. Exciton-dominated optical response of ultra-narrow graphene nanoribbons. *Nat. Commun.* **2014**, *5*, 4253.
(61) Havener, R. W.; Liang, Y.; Brown, L.; Yang, L.; Park, J. Van hove singularities and excitonic effects in the optical conductivity of twisted bilayer graphene. *Nano Lett.* **2014**, *14*, 3353−3357.
(62) Wang, S.; Kharche, N.; Costa Girão, E.; Feng, X.; Müllen, K.; Meunier, V.; Fasel, R.; Ruffieux, P. Quantum Dots in Graphene Nanoribbons. *Nano Lett.* **2017**, *17*, 4277−4283.